Nano Research
2023, 16(8): 11259–11268

ISSN 1998-0124 CN 11-5974/O4
https://doi.org/10.1007/s12274-023-5757-0

Research Article

Round-trip oscillation triboelectric nanogenerator with high output response and low wear to harvest random wind energy

Xinyu Hu[1,2], Junrui Feng[1,2], Chuangjian Liang[1], Heng Ning[1], Chunjin Chen[1], Jiayu Li[1], Honggui Wen[1], Huilu Yao[1], Lingyu Wan[1], and Guanlin Liu[1] (✉)

[1] *Guangxi Key Laboratory of Electrochemical Energy Materials, School of Physical Science and Technology, Guangxi University, Nanning 530004, China*

[2] *Beijing Institute of Nanoenergy and Nanosystems, Chinese Academy of Sciences, Beijing 101400, China*

© Tsinghua University Press 2023

Received: 6 January 2023 / **Revised:** 11 March 2023 / **Accepted:** 19 April 2023

ABSTRACT

Triboelectric nanogenerator (TENG) has made significant progress in wind energy harvesting. As the most advantageous rotary TENG among wind energy harvesters, the severe material wear and the output that fluctuates with wind speed seriously hinder the application of TENG wind energy harvesters. In this study, we propose a round-trip oscillation triboelectric nanogenerator (RTO-TENG) consisting of a crank transmission mechanism and a power generation unit. The RTO-TENG utilizes a simple crank transmission mechanism combined with a zigzag-laminated triboelectric nanogenerator (Z-TENG) to achieve high-performance constant output and low material wear. The crank transmission mechanism can realize the transformation from circular motion to arc reciprocating motion, converting the random wind energy into bi-directional kinetic energy, driving the vertical contact and separation of the Z-TENG. Due to the low transmission ratio (1:1) of the crank transmission mechanism and the consistent frequency of the Z-TENG contact–separation with that of the pendulum, the RTO-TENG's power generation unit (10 Z-TENGs) is insensitive to changes in wind speed, resulting in a constant and stable output response at various speeds. After 480,000 cycles, the output of RTO-TENG decreased by only 0.9% compared to the initial value of 6 μC, and the scanning electron microscopy (SEM) images of the polytetrafluoroethylene (PTFE) film showed no significant wear on the surface of the friction layer, demonstrating excellent output stability and abrasion resistance of the RTO-TENG wind energy collector's material. The equipped energy management module, based on a gas discharge tube switch, can further enhance the output performance of the RTO-TENG. After optimizing its inductor parameter *L* to match the load capacitor, it can charge a 220 μF load capacitor to 13.4 V in 40 s, resulting in a 298% improvement in charging speed compared to the voltage of 4.48 V without the management module. Therefore, the RTO-TENG can efficiently provide power to low-power small electronic devices for Internet of Things (IoTs), such as road traffic warning signs and thermo-hygrometers.

KEYWORDS

triboelectric nanogenerator, wind energy harvesting, round-trip oscillation structure, bi-directional kinetic energy, gas discharge tube switch

1 Introduction

The rapid development of Internet of Things (IoTs) technology has given rise to novel and convenient lifestyles, such as intelligent cities, intelligent homes, and intelligent healthcare. Data acquisition for such intelligence requires countless sensors [1–3], which rely on energy storage devices like batteries. However, the limited life of batteries, environmental pollution, high maintenance costs of equipment, and other defects are increasingly prominent, making it difficult for batteries to supply energy for future distributed sensors [4, 5]. Distributed energy solutions, that is, converting energy from the surrounding environment into electrical energy, have been recognized as safe, flexible, and environmentally sustainable energy development methods to solve the problem of traditional battery energy limitations [6, 7]. Distributed energy sources include thermal energy [8], wind energy [9, 10], solar energy [11], and acoustic energy [12]. Among these, wind energy is one of the most promising clean and renewable energy sources due to its wide distribution on the earth and abundant reserves [13–15]. Early wind energy collection methods relied on large electromagnetic generators (EMGs), which converted wind energy into mechanical work through the wind turbine, which was then converted into electrical energy by cutting magnetic induction lines through coils. This provided considerable grid-connected power generation energy in high-altitude regions with stable wind energy [16]. However, for small distributed low-power sensors, EMG is large, heavy in mass, and high installation costs, and their installation is limited by the geographical environment and other factors [17, 18]. They are not suitable for widely distributed IoT terminal sensors with small sizes and low power consumption. Triboelectric nanogenerator (TENG) provides an excellent solution to this problem because of their light mass, low cost, small size, easy installation, and portability [19–21]. Through

Address correspondence to guanlinliu@gxu.edu.cn

strenuous efforts of researchers worldwide, triboelectric nanogenerator can now harvest unstable wind energy to power small sensors to a certain extent.

Previous studies have shown that there are mainly two operation modes for TENG-based wind energy harvesters. The first is the vibro-driven contact–separation mode, which typically employs planar materials such as thin films [22, 23], fabrics [24, 25], and steel sheets [26]. With a parallel wind input, based on Bernoulli's principle, the faceted material vibrates, driven by the local pressure difference between the two sides, thus obtaining the relative motion and its kinetic energy. Different friction materials come into contact and separate from each other through external collision [22, 23, 26] or internal extrusion [24, 25], generating electrical energy in the external electrodes through the coupling of the frictional electrification effect and electrostatic induction effect [27]. This type of vibration-based TENG is durable owing to its contact–separation mode and can broaden the low-frequency bandwidth of wind energy collection. However, its output amplitude varies at different wind speeds with high instability [28, 29], making it difficult to adapt to the corresponding power management circuit to supply electronic devices with stable and continuous power [30, 31]. The second mode is the rotary TENG based on the free friction layer mode, which converts wind energy into rotational kinetic energy through windward structures, such as wind cups, before obtaining a constant and continuous high-output performance based on rotary TENG. However, this high performance comes at the cost of high material wear [32–34]. In previous studies, researchers typically optimized the friction materials [31, 35] and contact methods [36–38] of rotary TENGs to achieve wear reduction, for example, by using animal hair and other low-resistance materials as the friction layer or adopting soft contact between friction surfaces to reduce material wear by reducing frictional resistance. Automatic switching between the contact and non-contact modes is achieved through mechanical structures, reducing wear by reducing the contact friction time. However, the switching wind speed is high, and the output difference between the contact and noncontact modes is large, making the overall output fluctuate, which is extremely unfavorable for back-end applications [39]. Moreover, both material-optimized and structure-optimized rotary TENG fail to get rid of the mode of contact rotation between friction surfaces. The problem of material wear cannot be solved at the source. Therefore, we refer to this as the vibro-TENG vertical contact–separation mode. Based on the wind energy capture method of the rotary TENG wind energy harvester, we designed a triboelectric nanogenerator wind energy harvester that can achieve a constant high output and low wear under the excitation of random wind energy. We refer to this as the vibro-TENG vertical contact–separation mode. Our TENG has significant potential to capture wind energy with high efficiency.

In this study, we present a round-trip oscillation triboelectric nanogenerator (RTO-TENG) that utilizes a simple crank transmission mechanism in conjunction with a zigzag-laminated triboelectric nanogenerator (Z-TENG) to achieve high performance with constant output and low material wear. The RTO-TENG converts random wind energy into bi-directional kinetic energy and generates stable electrical energy through the power generation unit (10 Z-TENGs) by achieving back-and-forth vibration at a fixed angle. The RTO-TENG exhibited good mechanical regulation of random wind energy and a stable output response in different wind directions and speeds. As shown in Fig. 1(c), the crank transmission mechanism of the RTO-TENG consists of a rotor, a pendulum, and a fixing bolt. The rotor obtains continuous one-way rotational energy from the wind turbine, then transmits it to the pendulum through the fixing bolt below it to produce back-and-forth vibrations. The Z-TENG oscillates with the pendulum to achieve vertical contact and separation to produce electricity. After 480,000 cycles, the output was maintained at 99.1% of its initial value (6 μC). Therefore, the RTO-TENG is suitable for long and stable operations. With respect to the transmission process of the RTO-TENG, the transmission ratio of the rotor, pendulum, and Z-TENG is 1:1:1. In other words, when the rotor rotates for one week, the pendulum completes one cycle of oscillation, and the Z-TENG completes one contact separation driven by the pendulum. Therefore, the power generation unit of the RTO-TENG (10 Z-TENGs) is insensitive to the wind energy speed. This shows that the RTO-TENG exhibits good mechanical regulation of random wind energy and has a stable output response at various wind speeds. Several structural parameters, including arm length, wind cup size, and oscillation angle, were optimized to further improve the aerodynamic response and output performance of the RTO-TENG. The transfer charge quantity of the RTO-TENG reached up to 6 μC, and the short-circuit current reached 120 μA. The maximum instantaneous output power was 3.35 mW at a 2 MΩ matched load, which is sufficient to light up 978 commercial light-emitting device (LED) lamps. After the RTO-TENG was configured with a gas discharge tube (GDT)-based energy management circuit module, its charging capacity increased by 298%. Based on the high output of the RTO-TENG, it has the capability to drive electronic devices such as temperature hygrometers, electronic watches, and calculators, demonstrating its potential as a distributed energy source to provide sustainable power for small electronic devices on the Internet of Things and proposing a new strategy for the long-term stable harvesting of wind energy.

2 Results and discussion

2.1 Structure design and operator principle

Distributed energy technologies are widely applied as sustainable energy development solutions due to their security, efficiency, and flexibility. The RTO-TENG aims to provide sustainable and clean power to small electronic devices for the Internet of Things as an efficient, flexible, and long-lasting energy harvesting method. The prospective applications of the RTO-TENG in the fields of intelligent transportation and intelligent farms are displayed in the blueprint shown in Fig. 1(a). An RTO-TENG can be flexibly installed in intelligent farms and intelligent transportation systems as a distributed energy source to power small electronic devices. For example, an RTO-TENG can be installed on a fixed pole to illuminate road warning lights in intelligent traffic. The RTO-TENG could power a self-powered monitoring system on an intelligent farm. The mobile phone terminal of this monitoring system would receive information such as temperature and humidity from the thermo-hygrometers, and the pH value from the soil test pen via Bluetooth. When the soil moisture reaches a warning value, the phone will send a message to the automatic irrigation system to open the water valve. The RTO-TENG's constant output amplitude and long-time fatigue resistance under random wind energy driven conditions simplify the back-end matching circuit and make it easy to integrate. Moreover, the RTO-TENG enables the back-end application of small electronic equipment to be maintenance-free for a long time, thereby saving costs and expenses, and demonstrating the ability of the RTO-TENG to harvest random wind energy for self-driving systems.

The overall structure of the RTO-TENG, which includes the wind turbine, support frame, crank transmission module, and power generation unit, is shown in Fig. 1(b). The three wind

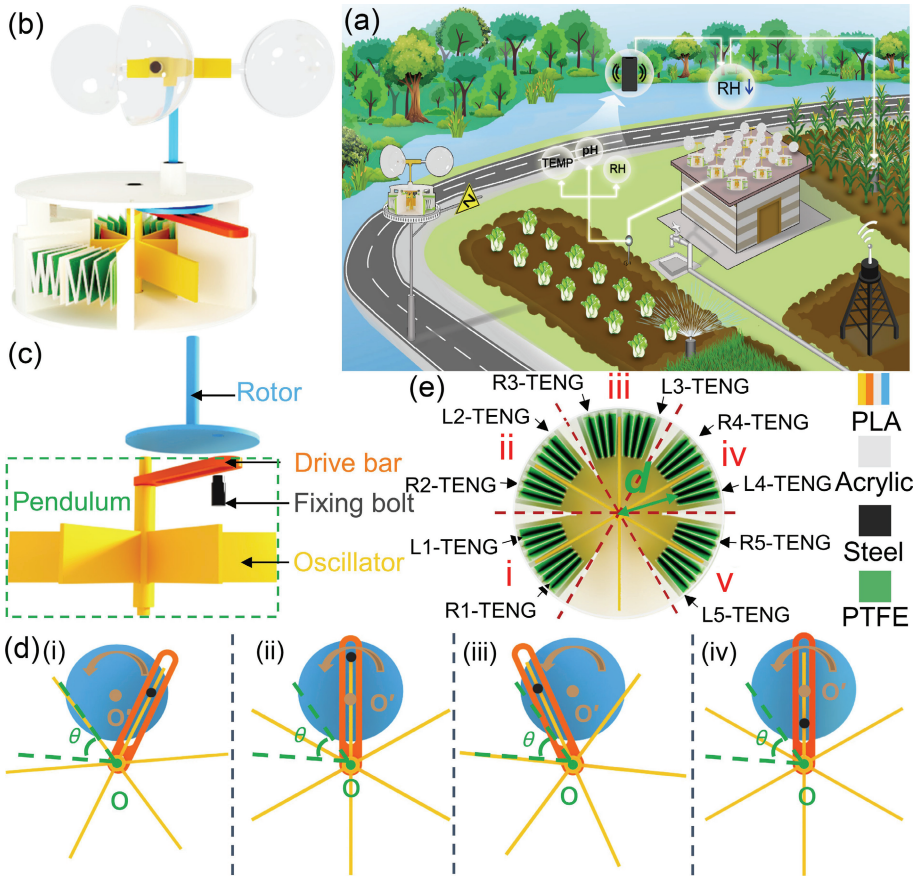

Figure 1 The round-trip oscillation structured triboelectric nanogenerator. (a) Schematic diagram of RTO-TENG application concept. (b) Schematic diagram of the overall structure. (c) The front view of the crank transmission mechanism. (d) One period of the oscillation process, (i) → (ii) → (iii) → (iv) → (i), while θ is the oscillation angle. (e) Relative positions of five basic units and schematic diagram of the station of TENG angle.

blades of the wind turbine are composed of acrylic tubes and acrylic hemispheres. The support frame (Figs. S1(a) and S1(b) in the ESM) is composed of an upper and lower substrate, with the upper substrate of the support frame having a circular platform at a distance *d* from the center of the substrate. The lower substrate has six uniformly distributed fan-shaped bases radially. The crank transmission module (Fig. 1(c) and Fig. S1(c) in the ESM) consists of a rotor, a fixing bolt, and a pendulum. As shown in Fig. 1(c), the drive bar and oscillator are embedded into a whole composition of the pendulum, the oscillator shaft is fixed in the central circular hole of the upper and lower substrates of the support frame, and the six blades of the oscillator fall into the six fan-shaped bases. The rotor shaft is fixed to the circular platform of the upper substrate of the support frame, and the upper end is fixed to the wind turbine. There is a small hole at the edge of the rotor to install the fixing bolt, and the fixing bolt on the rotor is placed in the narrow slot of the drive bar and can freely slide in the slot. The power generation unit consisted of ten Z-TENGs. The Z-TENG (Figs. S1(d) and S1(e) in the ESM) was constructed from a polytetrafluoroethylene (PTFE) substrate and 14 spring steel electrodes. Seven spring steel electrodes were attached to the PTFE film on one side, and the remaining spring steel electrodes were untreated. The seven PTFE-spring steel electrodes and seven spring steel electrodes were alternately attached to the two sides of the zigzag PTFE substrate to form a Z-TENG. Subsequently, the ten Z-TENGs were placed on the left and right sides of the oscillator blade at the i, ii, iii, iv, and v sector bases displayed in Fig. 1(e), with each Z-TENG labeled accordingly. The Z-TENGs located on the left side of the oscillator blades at the i, ii, iii, iv, and v sectors are labeled as L1-TENG, L2-TENG, L3-TENG, L4-TENG, and L5-TENG. The Z-TENGs on the right side are labeled as R1-TENG, R2-TENG, R3-TENG, R4-TENG, and R5-TENG. One end of the Z-TENG was attached to the fan-shaped base, and the other was attached to the oscillator blade, thus realizing coupling of the contact–separation motion of the Z-TENG with the oscillation motion of the oscillator. Driven by the random wind energy, the rotor and the fixing bolt on it rotate in one direction driven by the wind turbine, and the bolt slides back and forth in the drive bar slot, thus driving the oscillator to oscillate back and forth with an angle of θ, converting the random wind energy into the bi-directional kinetic energy of the oscillator. The blades of the oscillator oscillate back and forth in the fan-shaped base of the lower substrate while driving the Z-TENG contact and separation, thereby converting the bi-directional kinetic energy into electrical energy. The detailed transmission process is shown in Fig. 1(d), wherein it is indicated that the rotor turns counterclockwise. The rotor and its fixing bolt move through the i-ii-iii motion path, thereby driving the pendulum swing to the left. The 5 TENGs (L-TENG) located on the left side of the oscillator blade transitioned from the separation state to the contact state. The five TENGs (R-TENG) located on the right side of the oscillator blade changed from a contact to the separate state. Subsequently, the rotor continued to rotate and the fixing bolt moved through the path of iii-iv-i, driving the pendulum swing to the right. L-TENG changed from the contact state to the separated state, and R-TENG changed from the separated state to the contact state. After several swing cycles, the charge distribution and current flow of the L-TENG and R-TENG during the operation are shown in Fig. 2(a). Owing to the difference in the electron-binding ability of the PTFE film and spring steel electrode, the PTFE film carries a negative charge, and the spring steel electrode carries an equivalent positive charge. When the oscillator vibrated from the left side of the base to the right side, the L-TENG changed from the contact state to the separated state,

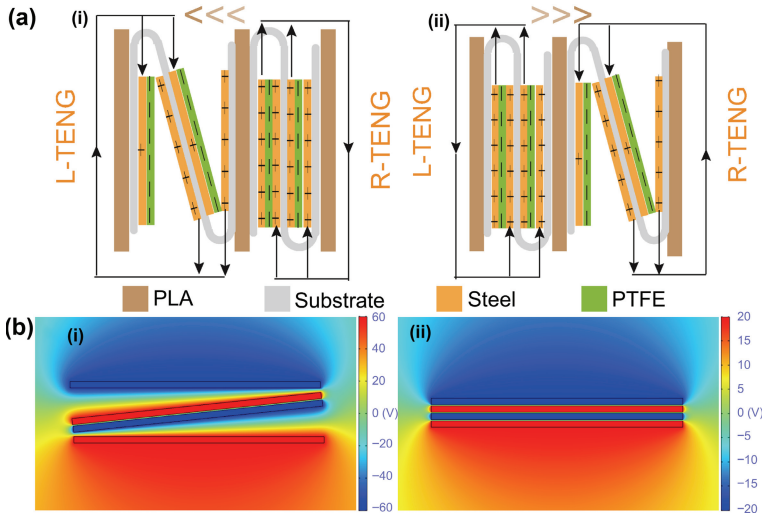

Figure 2 Schematics of the working mechanism of RTO-TENG. (a) Schematic illustrations of the charge distribution. (b) Potential distribution by COMSOL was employed to elucidate the working principle of RTO-TENG, (i) the separate state and (ii) the contact state.

and the potential at both the PTFE-spring electrode and spring steel electrode changed. The electrons flowed from the spring steel electrode to the PTFE-spring steel electrode through the external circuit to balance the change in potential difference. The generated current flowed from the PTFE-spring steel electrode to the spring steel electrode through an external circuit. When the oscillator vibrated from the right side of the base to the left side, the L-TENG changed from a separated state to a contact state, and the electron and current flows of L-TENG and R-TENG were opposite to those of the front one. During continuous oscillation, the L-TENG and R-TENG produced alternating currents in opposite directions. Finite-element simulations of the potential distribution were performed using COMSOL, as shown in Fig. 2(b), and the results are consistent with the above analysis.

2.2 RTO-TENG structural parameter optimization

The oscillation angle θ (Fig. 3(a)) and the distance (Fig. 1(c)) of the inner side of the Z-TENG from the center of the base d are two key factors that determine the output performance of the RTO-TENG. We systematically investigated the effects of these two factors using the control parameter method. First, the oscillation angle was considered.

$$\theta = 2\arctan\frac{T}{R} \quad (1)$$

where T is the rotation radius (the distance between the center of the rotor and the fixing bolt, i.e., AO') and R is the distance from the center of the rotor to the center of the oscillator (i.e., OO'). According to Eq. (1), it can be inferred that the oscillation angle θ positively correlates with the T. Therefore, the oscillation angle θ can be characterized by the bolt T. Figure 3(b), and Figs. S2(a) and S2(b) in the ESM illustrate the output performance of L1-TENG and R1-TENG measured at different T (16–20 mm and Δ = 1 mm) under 3 m/s wind energy drive, respectively. The open-circuit voltage, short-circuit current, and transferred charge of L1-TENG and R1-TENG gradually increased with an increase in T when the T was between 16 and 18 mm. The output performance of L1-TENG and R1-TENG exhibited a decreasing trend when the T was between 18 and 20 mm. This is because the increase of the T causes the growth of the oscillation angle θ when the oscillator oscillates in the 60° sector base unit. However, the contact–separation angle (60°–θ) of the Z-TENG decreases, and the contact surfaces are not entirely separated from each other with insufficient charge transfer, thus reducing the output performance.

Subsequently, to further optimize the output performance of the TENG, the contact–separation distance of the Z-TENG was varied by adjusting the distance d of the inner side of the Z-TENG from the center of the base. Figure 3(c), and Figs. S3(a) and S3(b) in the ESM demonstrate the output performance of L1-TENG and R1-TENG measured at different distances d (50–90 mm and Δ = 5 mm) under 3 m/s wind energy drive, respectively. With an increase in distance d, the output performance of L1-TENG and R1-TENG did not exhibit a linearly increasing trend, but increased first and then decreased. At d = 70 mm, the transfer charge and short-circuit current of L1-TENG and R1-TENG reached a peak, and the transfer charge and short-circuit current of L1-TENG were 716 nC and 9.45 μA, respectively. This is because the Z-TENG contact–separation distance is proportional to the distance d. When d is too small, the Z-TENG cannot open completely. When the distance d is too large, the stretching range of the Z-TENG is too extensive. The film substrate lacks sufficient rigidity to resist the effect of gravity; therefore, the substrate sags, which causes a few contact surfaces to be incompletely separated, resulting in a lower output. For the RTO-TENG to effectively collect wind energy, a T of 18 mm and a distance of the inner side of the Z-TENG from the center of the base d of 70 mm were selected.

2.3 Optimization of wind turbine structure parameters

We optimized the wind turbine parameters on the experimental platform, as shown in Fig. S3(c) in the ESM, to ensure the stable operation of the RTO-TENG in a wind energy environment. We used a blower to simulate wind energy at different wind speeds and measured the start-up wind speed and real-time rotational speed of the wind turbine with varying parameters using an anemometer and a non-contact tachometer.

As a critical part of energy capture, the structural parameters of the wind turbine (Fig. S3(d) in the ESM) inevitably affect the aerodynamic performance of the entire energy collection device [40]. In addition, the Z-TENG in the power generator unit affects the aerodynamic performance of the energy collection device owing to the resistance force to contact and stretch that exists during the transmission process, as well as the frictional moment M_a of the transmission components. The start-up wind speed, which is defined as the minimum wind speed required to rotate the wind cup from rest to rotation, is usually used to characterize the aerodynamic performance. It depends on several factors, including the structural parameters of the wind turbine, the friction torque M_f of the transmission components themselves,

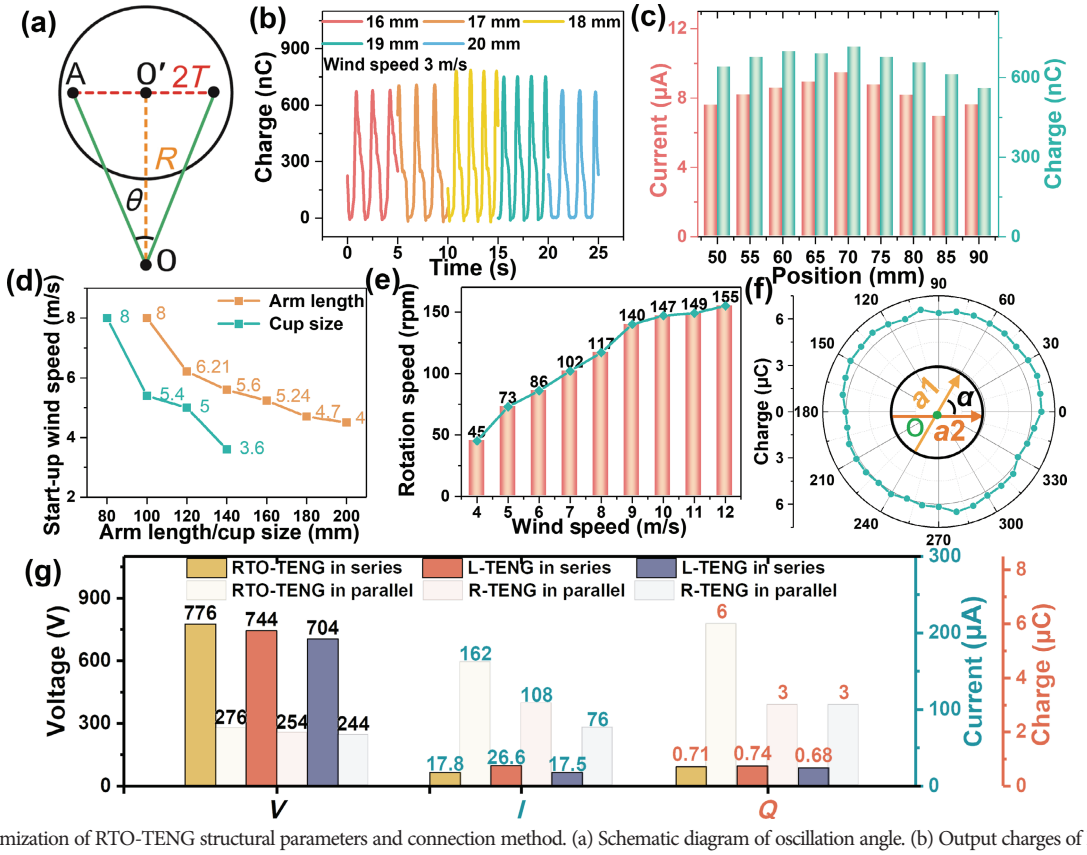

Figure 3 Optimization of RTO-TENG structural parameters and connection method. (a) Schematic diagram of oscillation angle. (b) Output charges of L1-TENG for various rotation radius at d = 70 mm. (c) Output performance of L1-TENG for various position at T = 18 mm. (d) Start-up speed of wind turbine with various arm lengths and various wind cup sizes. (e) Relationship between the rotation speed and wind speed for the arm length of 160 mm and the wind cup size of 120 mm. (f) RTO-TENG output charge under different response angles. (g) Comparison of the output performance of RTO-TENG, L-TENG, and R-TENG in series and parallel without rectification, the rotation speed is 150 rpm.

and the load torque M_a brought about by the contact–separation process of the Z-TENG. The driving force F_D corresponds to the start-up wind speed

$$F_D = F_t - F_r \tag{2}$$

where F_t is the total thrust received by the wind turbine and F_r is the total resistance obtained by the wind turbine. The force on a single wind cup is divided into two conditions: wind energy acting on the concave surface as thrust F_1 and wind energy acting on the convex surface as resistance F_2

$$F_1 = \frac{1}{2}\rho S(V_\tau - v)^2 C_1 \tag{3}$$

$$F_2 = \frac{1}{2}\rho S(V_\tau + v)^2 C_2 \tag{4}$$

where ρ is the air density, S is the force area of the wind cup, V_τ (this calculation equation is shown in Note S1 in the ESM) is the velocity component of wind speed V in the tangential direction, v (its calculation equation shown in Note S1 in the ESM) is the rotational line velocity at the midpoint of the wind cup, and C_1 and C_2 are the concave convex face drag coefficients, respectively. The wind turbine starts when the driving torque generated by the driving force F_D acting on the wind turbine can overcome the load torque M_a and friction torque M_f. The torque at this time is called the start-up torque M_0

$$\overrightarrow{M_0} = \overrightarrow{F_D} \times \overrightarrow{L} = \overrightarrow{M_a} + \overrightarrow{M_f} \tag{5}$$

where L is the length of the wind arm (the distance from the center of rotation to the point of force action). Figure 3(d) illustrates the start-up wind speed of the wind turbine (Fig. S4(a) in the ESM) with different arm lengths L (100–200 mm and Δ = 20 mm). With the start-up torque M_0 remaining constant, the required driving force F_D of the wind turbine decreased as the length of the wind arm increased. Accordingly, the required start-up wind speed of the wind turbine decreased, and a wind arm with a length of 160 mm was selected after considering the floor space and start-up wind speed.

With a constant wind-turbine arm length of 160 mm, the start-up torque M_0 was maintained, and the required driving force F_D of the wind turbine remained constant. Figure 3(d) shows the start-up wind speeds of the wind turbine with wind cup diameters of 80, 100, 120, and 140 mm (Fig. S4(b) in the ESM). The start-up wind speed of the wind turbine decreased as the diameter of the wind cup gradually increased. This is because the force area of the wind cup is proportional to its diameter and an increase in the wind cup diameter causes an increase in the force area of the wind cup. The start-up wind speed of the wind turbine decreased when driving force F_D remained invariant. Although the wind turbine with a wind cup diameter of 140 mm had a low start-up wind speed, a wind cup with a diameter of 120 mm was adopted because of the size limitation of the RTO-TENG.

After optimizing the wind turbine parameters, we determined that a wind turbine with a wind arm length of 160 mm and a wind cup diameter of 120 mm was suitable for investigating the relationship between the rotational speed and wind speed. The relationship curve is shown in Fig. 3(e). A linear relationship exists between wind speed and rotational speed at 4–9 m/s. Beyond 9 m/s, the rotational speed tends to increase slowly because the general trend is to increase the rotational speed with an increase in wind speed before the blade angle of attack reaches the stall angle. However, when the wind speed exceeded the threshold value (9 m/s), the wind blade deformation caused the blade angle of attack to change, and the rotor speed increase slowed down.

In addition, an optimized vertical-axis wind-cup wind turbine was employed to verify that it has a stable horizontal output response to the wind in all directions. The response angle α of the wind energy collector was sequentially increased from α = 0° to α = 360° (at 10° intervals). The response angle α is defined as the angle between the wind direction and the horizontal radial direction of the wind energy collector base (Fig. 3(f)). The output performance of the RTO-TENG measured at each response angle at a wind speed of 7 m/s is shown in Fig. 3(f) and Fig. S5(a) in the ESM. The charge, current, and voltage curves do not fluctuate much, with charge fluctuation under 50 nC, voltage fluctuation under 20 V, and current fluctuation under 16 μA. This demonstrates that the RTO-TENG has a stable output response to wind energy in all directions. Its operation has minimal dependence on the wind direction, making it suitable for collecting wind energy in all horizontal directions.

2.4 Influence of the connection method of Z-TENG on the output performance of RTO-TENG

To ensure that the RTO-TENG operates with a stable excitation source, we employed a servomotor (Fig. S6(a) in the ESM) as the driving source. Under the drive of a servomotor, we optimized the connection of the RTO-TENG and tested its stability, durability, and load matching.

The connection method between the output electrodes of each Z-TENG played a vital role in the output performance of the RTO-TENG. First, without a connected rectifier bridge, the L-TENG, R-TENG, and RTO-TENG were connected in series and parallel. The differences in the output performance of the L-TENG, R-TENG, and RTO-TENG (see Fig. S7(a) in the ESM for the output of a single Z-TENG) with series and parallel connections were investigated. Figure S8(a) in the ESM shows the connection method of the RTO-TENG in series, where the negative electrodes of the L-TENG and R-TENG were connected in series. Figure S8(b) in the ESM illustrates the RTO-TENG parallel connection method, in which the positive and negative electrodes of the L-TENG are connected in parallel with the negative and positive electrodes of the R-TENG. This is because the L-TENG and R-TENG in the RTO-TENG have different frequencies, and the R-TENG was in a separate state when the L-TENG was in contact. There exists a phase difference of π between the two outputs, and the direct series and parallel connection will cause the output of RTO-TENG to offset. Therefore, the RTO-TENG was connected in series and parallel, as shown in Figs. S8(a) and S8(b) in the ESM to avoid an output offset. Driven by a rotational speed of 150 rpm, the output performance of the L-TENG (Fig. S9(a) in the ESM), R-TENG (Fig. S9(b) in the ESM), and RTO-TENG (Fig. S9(c) in the ESM) in series and parallel without a rectifier bridge were measured, as shown in Fig. 3(g). The output currents and transferred charges of the L-TENG, R-TENG, and RTO-TENG in the parallel connection were more significant than those in the series connection; however, their voltages were smaller. The output current of RTO-TENG in parallel reached 160 μA, and the transferred charge reached 6 μC. The contact separation state of each contact surface of the Z-TENG was not synchronized. Therefore, the phase difference between the L-TENG and R-TENG is not constant, which makes the phase difference between the electrical signal output frequencies of the L-TENG and R-TENG inconsistent with large fluctuations. This causes the voltage of the RTO-TENG to be unequal to the sum of the voltages of the L-TENG and R-TENG. In addition, the output of L-TENG is higher than that of R-TENG because when the servomotor provides the torque for clockwise steering, the motion path of the fixing bolt is i-ii-iii when steering the L-TENG. When driving the R-TENG, the motion path of the fixing bolt is iii-iv-i. The distance between the fixing bolt and the oscillation center in the i-ii-iii motion path is greater than the distance between the fixing bolt and the oscillation center in the iii-iv-i motion path. Therefore, the torque of turning to the L-TENG is larger than that of turning to the R-TENG, and the force acting on the L-TENG is also larger than that on the R-TENG.

Second, we investigated the output differences between the L-TENG, R-TENG, and RTO-TENG when connected in series and parallel after rectification using the rectifier bridge. As shown in Figs. S10(a) and S10(b) in the ESM, the output differences of the L-TENG, R-TENG, and RTO-TENG with series and parallel connections after connecting with the rectifier bridge were comparable to those without the rectifier bridge. However, after rectification, the voltages of the L-TENG, R-TENG, and RTO-TENG in series and parallel were lower than those without the rectifier bridge because the rectifier bridge itself had losses that caused a voltage drop. After the rectification, the parallel voltage of the RTO-TENG was 148 V.

Moreover, wind energy is inherently random and irregular, posing significant challenges for wind energy collection. It is crucial to determine whether the wind energy collector can adapt to spontaneous wind energy to generate a stable power output to provide a reliable energy supply for back-end equipment. The crank transmission mechanism of the RTO-TENG designed in this study has a low transmission ratio (1:1) with good mechanical regulation capability for random wind energy; that is, the power generation unit (10 Z-TENGs) can generate constant and stable electricity driven by random wind energy. Therefore, we further investigated the stability of the RTO-TENG output performance under different wind energies using three distinct excitation methods (Fig. 4(a)(i)): the first, random step input, where the motor speed varied in the interval [50, 200] rpm within 25 s; the second, stepwise incremental input, where the motor speed gradually increased linearly from 0 to 250 rpm within 25 s; and the third, constant input, where the motor speed maintained at 150 rpm within 25 s. Under the excitation method of random step input (Figs. 4(b)(i) and 4(b)(ii)) and stepwise incremental input (Figs. S11(a)(i) and S11(a)(ii) in the ESM), the transfer charge and open-circuit voltage output curves of RTO-TENG at different wind speeds have different densities. However, the amplitude of the output curve fluctuation was small, without any apparent fluctuations, and the transfer charge and open-circuit voltage were maintained at 6 μC and 220 V, respectively. Using the excitation method with constant input (Figs. S11(b)(i) and S11(b)(ii) in the ESM), the transfer charge and open-circuit voltage output curves of the RTO-TENG also do not fluctuate significantly. The output of the RTO-TENG remained equal to that of the random step input and stepwise incremental input excitation methods. These regularities under the three excitation methods demonstrate that the RTO-TENG has a constant high-output response to wind energy at different wind speeds. Therefore, the low-transmission-ratio crank transmission mechanism of the RTO-TENG demonstrated good adaptability to random wind energy.

Material wear is the main factor that causes the degradation of output performance. In this study, the oscillating structure was designed to be free of the traditional rotating TENG contact working mode to achieve vertical contact separation of the TENG, which can avoid material wear to a certain extent and maintain the high output of the TENG. Figure 4(c) illustrates that after 480,000 cycles, the transferred charge of the RTO-TENG decreased by only 0.9% compared to 6 μC in the initial case. The SEM image of the PTFE after 480,000 cycles (Fig. 4(d)) was compared with the SEM image of the unused PTFE (Fig. 4(e)), revealing no significant wear. This demonstrates that the design of the oscillating structure provides the RTO-TENG with good wear

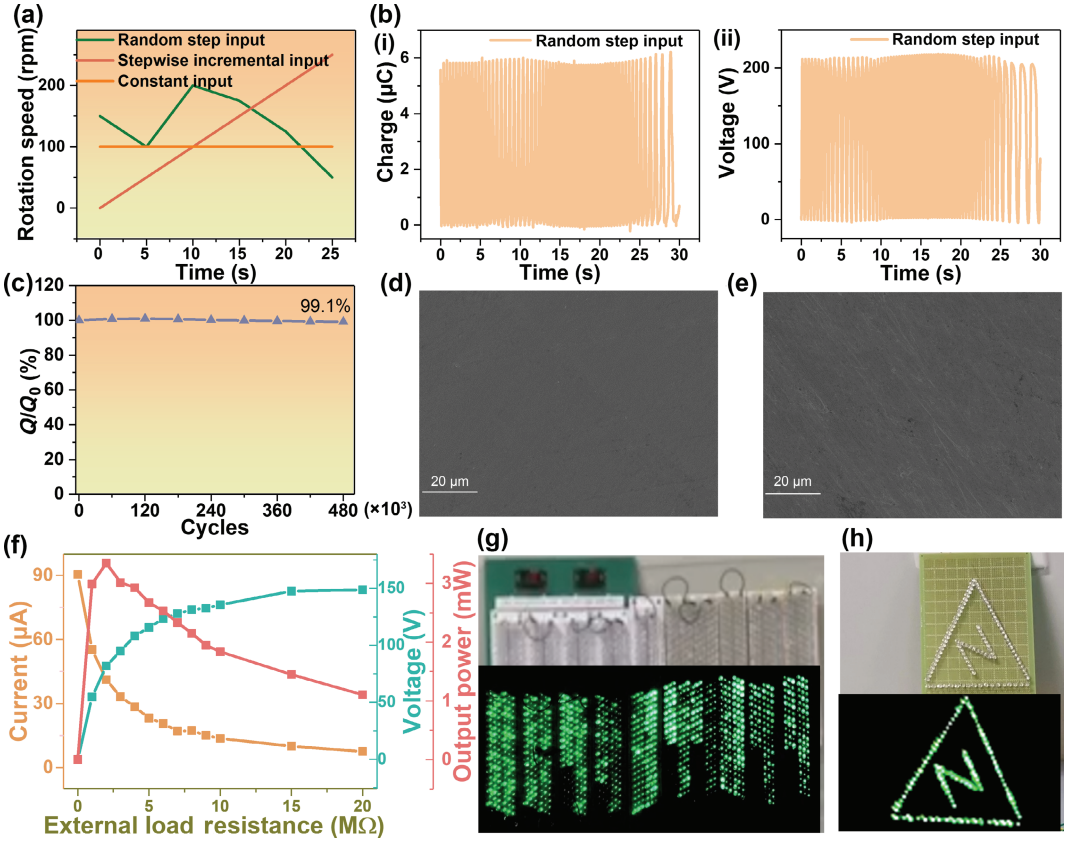

Figure 4 Stability test and durability test of RTO-TENG and explore the different connection modes of each Z-TENG. (a) Three different excitation methods: random step input, constant input, and stepwise incremental input. (b) Output performance of random step input. (c) Durability test of RTO-TENG with 480,000 operation cycles, the rotation speed is 150 rpm. SEM images of PTFE (d) at the initial situation and (e) after 480,000 operation cycles, the scale bar is 20 μm. (f) Output current resistance, output voltage resistance, and output power resistance of the RTO-TENG. (g) The 978 LEDs and (h) road sign powered by RTO-TENG.

resistance to ensure a high output even after long operation. In addition, as shown in Table S1 in the ESM, the RTO-TENG has excellent wear resistance and output performance compared to other rotary TENG.

Based on the stable high output of the RTO-TENG, each Z-TENG generation unit of the RTO-TENG was connected in parallel after rectification in the resistance-matching test. Figure 4(f) displays the voltage, current, and power curves of the RTO-TENG under different matched loads measured at 100 rpm. With the increase of load, the current drops rapidly, then flattens out, while the voltage exhibits the opposite behavior, and the instantaneous output power increases and then decreases. The maximum instantaneous output power is 3.35 mW at a 2 MΩ matched load.

To demonstrate the commercial potential of the RTO-TENG, it was driven by wind energy with a simulated wind speed of 7 m/s using a blower. The rectified RTO-TENG (Fig. S12(a) in the ESM) was able to light up 978 commercial LED lights in series (Fig. 4(g) and Video ESM1). It can also drive traffic road warning lights (Fig. 4(h) and Video ESM2) to provide a warning for drivers operating at night to ensure driving safety. This is expected to be applied in the field of intelligent transportation to power low-power electronic devices.

2.5 Application

Matching the energy management circuit of an RTO-TENG is essential for improved energy harvesting from random wind energy. In this study, a low-loss GDT was employed as a self-control switch for the energy management circuit (Fig. 5(a)). When the GDT switch is closed, the power generated by the front-end RTO-TENG accumulates in the storage capacitor C_0. The GDT switch automatically opens when the voltage across storage capacitor C_0 reaches the GDT breakdown voltage to release the accumulated power in the storage capacitor C_0 instantaneously to achieve voltage reduction and current increase, thus increasing the charging speed of load capacitor C_1. Figure 5(b) shows that the output current of the RTO-TENG was 2.1 mA after energy management. The accumulator capacitor C_0 and inductor L were further optimized experimentally to maximize the energy management circuit function. Figure 5(c)(i) demonstrates the charging curves of 220 μF load capacitor C_1 under different storage capacitors C_0. The charging voltage of load capacitor C_1 is highest at 60 s with capacitor C_0 = 3.3 nF. Therefore, the optimal storage capacitor C_0 was selected as 3.3 nF. Figure S13(a) in the ESM and Fig. 5(c)(ii) demonstrate the charging curves of load capacitor C_1 with 47 and 100 μF at different inductors L, respectively. When the inductance L = 470 μH, the 47 μF load capacitor C_1 charges to 10 V in the shortest time. When the inductance L = 220 μH, the 100 μF load capacitor C_1 charges 10 V in the shortest time. It indicates that the fastest charging rate of load capacitor C_1 is obtained with the best-matched inductor L. Subsequently, the saturation voltages V_1 obtained with 47, 100, 220, and 470 μF capacitor C_1 after matching the optimal inductor L (see Table 1 for the corresponding saturation time) were compared with the voltages V_0 (Table 1) of 47, 100, 220, and 470 μF load capacitor C_1 without the gas discharge tube in the corresponding saturation time, and the results shown in Fig. 5(d) and Fig. S13(b) in the ESM.

In a wind environment with a simulated wind speed of 7 m/s using a blower, the RTO-TENG, after being modulated by the gas discharge tube energy management circuit, dramatically boosted the speed of its charging load capacitor C_1 and shortened its charging time of load capacitor C_1, thus effectively improving the wind energy conversion efficiency. The RTO-TENG can charge a

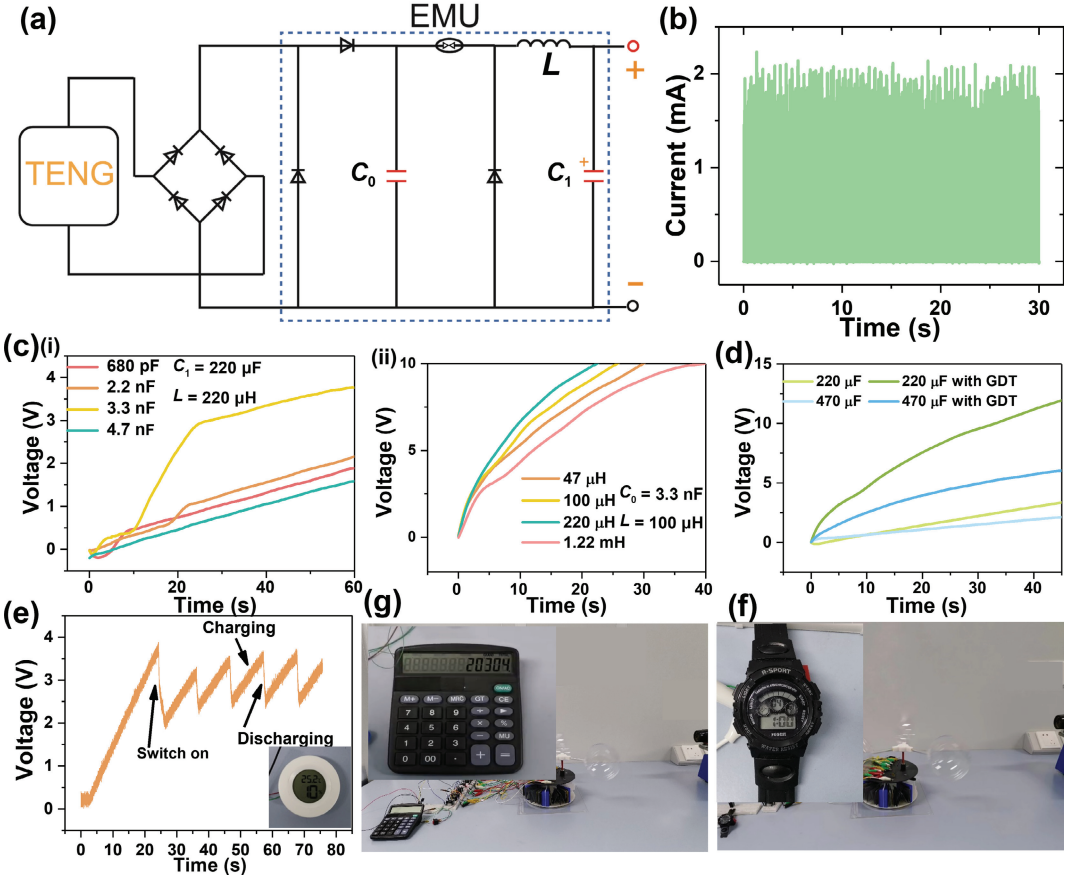

Figure 5 Demonstrating performance of RTO-TENG. (a) Circuit diagram of the RTO-TENG with GDT. (b) Current of RTO-TENG after GDT EMU. (c)(i) Voltage curves of 220 μF capacitor C_1 at 100 rpm rotation speed with different capacitors C_0 of GDT circuit, the rotation speed is 100 rpm, and (c)(ii) voltage curves of 100 μF capacitor C_1 at 100 rpm rotation speed with different inductance L of GDT circuit, the rotation speed is 100 rpm. (d) Comparison of voltage curves of 220 and 470 μF capacitors C_1 with and without GDT. (e) Voltage–time curve of temperature hygrometers at 7 m/s wind speed and real photographs of the temperate and humidity meter. Physical photographs of (g) calculator and (f) digital watch powered by RTO-TENG and 7 m/s wind speed.

Table 1 Comparison of the voltage of capacitor C_1 with and without the gas discharge tube

Capacitor (μF)	V_0 (V)	V_1 (V)	Saturation time (s)	V_1/V_0 (100%)
47	16.9	19.2	40	113
100	6.7	12.8	45	189
220	4.5	13.4	60	297
470	2.8	6.7	60	248

220 μF load capacitor C_1 to 5 V within 11 s, which effectively and quickly drives small electronic devices such as temperature hygrometers (Fig. 5(e) and Video ESM3), a calculator (Fig. 5(g) and Video ESM4), and an electronic watch (Fig. 5(f) and Video ESM5). The charging and discharging curves of the temperature hygrometers are shown in Fig. 5(e). After the load capacitor C_1 is discharged, the RTO-TENG can quickly charge the load capacitor C_1 with the assistance of the GDT energy management circuit to reach the nominal operating voltage of the temperature hygrometers. This demonstrates that the RTO-TENG, after integrating with the GDT energy management circuit, can serve as a distributed and sustainable energy source to continuously power small electronic devices of the IoT.

3 Conclusions

In summary, the crank transmission mechanism used in this structure achieves back-and-forth vibrations at a fixed angle, allowing for the conversion of random wind energy into kinetic energy in both directions of the oscillator through the rotor. At 480,000 cycles, the output of the RTO-TENG only decreased by 0.9% compared to the initial value of 6 μC, and the PTFE film surface showed minimal wear in the SEM image. In addition, the RTO-TENG's transmission module had a low transmission ratio, and its power generation units (10 Z-TENG) exhibited low fluctuations in output response to wind energy at different wind speeds. Therefore, to a certain extent, the RTO-TENG addresses the issues of material wear and output performance fluctuations with wind speed that the traditional rotor structure can cause. After being managed by a GDT energy management circuit, the RTO-TENG can drive electronic meters, calculators, and temperature hygrometers, making it an effective distributed energy source for small electronic devices in the IoT.

4 Experimental sections

4.1 Fabrication

4.1.1 Fabrication of the RTO-TENG

The RTO-TENG comprised a wind turbine, support frame, crank mechanism, and 10 Z-TENGs. The support frame was fabricated

by three-dimensional (3D) printing (Tiertime UP300) with polylactic acid (PLA) and was a cylindrical base with a diameter of 198 mm and a height of 80 mm. The base was divided into six sectors by six radially-shaped sectors with a radius of 50 mm and an angle of 20° (the sector angle is 60°).

4.1.2 *Fabrication of crank mechanism*

The crank mechanism included a rotary disk, drive bar, fixing bolt, and oscillator. Except for the fixing bolt, which was made of metal, the rest were 3D printed using PLA. A rotor with a diameter of 50 mm, thickness of 3 mm, and height of 80 mm. A 3 mm diameter hole at a distance T (T = 16, 17, 18, 19, and 20 mm) from the center of the turntable was used to mount a spring steel fixing bolt with a height of 15 mm. The T of the fixing bolt was adjusted to control the oscillation angle θ.

4.1.3 *Fabrication of the power generation unit*

The power generation unit consisted of 10 Z-TENGs. The Z-TENG employed a 50 μm thick PTFE film with a width of 50 mm as the substrate, which was folded into a zigzag substrate with seven layers. Fourteen pieces of spring steel sheets measuring 40 mm × 50 mm × 40 μm were cut to make electrodes. Seven spring steel sheets were attached with an 80 μm thick PTFE film, and the remaining 7 sheets were left untreated. The spring steel sheets with and without the film were alternately attached to the PTFE film substrate on the front and back sides, and then the electrodes with and without the film were connected in parallel with wires, respectively.

4.1.4 *Fabrication of the wind turbine*

The central connecting component of the wind turbine was 3D printed in PLA with a diameter of 35 mm and a height of 18 mm. Three small holes with a diameter of 7 mm and a depth of 15 mm were distributed radially (120° apart) to fix the wind blade, and a small hole with a diameter of 8 mm and a depth of 8 mm was used to fix the rotor shaft. An acrylic tube with an outer diameter of 7 mm was cut into sizes of 40, 60, 80, 100, 120, and 140 mm × 3, along with a 120 mm diameter acrylic hemisphere to form wind turbines with blade lengths of 100, 120, 140, 160, 180, and 200 mm × 3 to investigate the effect of wind arm length on start-up wind speed. Acrylic hemispheres with diameters of 40, 60, 80, 100, 120, and 140 mm × 3 were combined with acrylic tubes with lengths of 140, 130, 120, 110, 100, and 90 mm × 3 and outer diameters of 7 mm to form a wind turbine with a blade length of 160 mm to investigate the effect of wind cup size on the start-up wind speed.

4.2 Data measurement

To simulate the effect of wind energy on the wind cup, servomotors (Ympc, 60st-mo1930) were used to provide rotational motion at different speeds. The wind blower was used to simulate wind energy in a natural environment. The start-up wind speed of the wind turbine was measured using an anemometer (AS-H6), and the rotor speed was measured using a noncontact tachometer (TRSI TA8146A). Charge, current, and voltage were measured using an electrostatic meter 6514 (Keithley, 6514). The high-voltage output was measured using an oscilloscope (Tektronix MDO3012) and a high-voltage probe (Tektronix P6015A). The potential distribution of the Z-TENG in the separated and contact states was simulated using COMSOL (COMSOL Multiphysics 5.4).

Acknowledgements

The research was supported by the Natural Science Foundation of Guangxi Province (No. 2021GXNSFAA075009), the Specific Research Project of Guangxi for Research Bases and Talents (No. GUIKEAD22035178), and the National Key R&D Project from Minister of Science and Technology (No. 2021YFA1201603).

Electronic Supplementary Material: Supplementary material (additional figures and videos, including the lateral view of the energy conversion module. The output performance of L1-TENG and R1-TENG with various T and distance d. Physical photographs of wind turbines with different arm lengths and cup sizes. The output charges of RTO-TENG under different response angles. The output performance of single Z-TENG. Physical photograph of the measurement system. Comparison of the output performance of L-TENG, R-TENG, and RTO-TENG in series and parallel. Connection of RTO-TENGs in parallel and parallel without rectifier bridge. Comparison of the output performance of RTO-TENG in series and parallel after rectification. Stability test of the RTO-TENG. Circuit diagram of RTO-TENG light LEDs. Voltage curves of 47 μF capacitor with different inductance L. Comparison of voltage curves of 47 and 100 μF capacitors with and without GDT) is available in the online version of this article at https://doi.org/10.1007/s12274-023-5757-0.

References

[1] Wang, Z. L.; Chen, J.; Lin, L. Progress in triboelectric nanogenerators as a new energy technology and self-powered sensors. *Energy Environ. Sci.* **2015**, *8*, 2250–2282.

[2] Liu, L.; Guo, X. G.; Lee, C. Promoting smart cities into the 5G era with multi-field Internet of Things (IoT) applications powered with advanced mechanical energy harvesters. *Nano Energy* **2021**, *88*, 106304.

[3] Wang, J. J.; Cui, P.; Zhang, J. J.; Ge, Y.; Liu, X. L.; Xuan, N. N.; Gu, G. Q.; Cheng, G.; Du, Z. L. A stretchable self-powered triboelectric tactile sensor with EGaIn alloy electrode for ultra-low-pressure detection. *Nano Energy* **2021**, *89*, 106320.

[4] Wang, Z. L. Triboelectric nanogenerators as new energy technology and self-powered sensors—Principles, problems and perspectives. *Faraday Discuss.* **2014**, *176*, 447–458.

[5] Liu, G. L.; Guo, H. Y.; Chen, L.; Wang, X.; Wei, D. P.; Hu, C. G. Double-induced-mode integrated triboelectric nanogenerator based on spring steel to maximize space utilization. *Nano Res.* **2016**, *9*, 3355–3363.

[6] El-Khattam, W.; Salama, M. M. A. Distributed generation technologies, definitions and benefits. *Electr. Power Syst. Res.* **2004**, *71*, 119–128.

[7] Wang, Z. L. Entropy theory of distributed energy for Internet of Things. *Nano Energy* **2019**, *58*, 669–672.

[8] Liu, G. L.; Chen, J.; Guo, H. Y.; Lai, M. H.; Pu, X. J.; Wang, X.; Hu, C. G. Triboelectric nanogenerator based on magnetically induced retractable spring steel tapes for efficient energy harvesting of large amplitude motion. *Nano Res.* **2018**, *11*, 633–641.

[9] Liu, G. L.; Liu, R. P.; Guo, H. Y.; Xi, Y.; Wei, D. P.; Hu, C. G. A novel triboelectric generator based on the combination of a waterwheel-like electrode with a spring steel plate for efficient harvesting of low-velocity rotational motion energy. *Adv. Electron. Mater.* **2016**, *2*, 1500448.

[10] Wang, Y.; Chen, T. Y.; Sun, S. W.; Liu, X. Y.; Hu, Z. Y.; Lian, Z. H.; Liu, L.; Shi, Q. F.; Wang, H.; Mi, J. C. et al. A humidity resistant and high performance triboelectric nanogenerator enabled by vortex-induced vibration for scavenging wind energy. *Nano Res.* **2022**, *15*, 3246–3253.

[11] Wu, Y. C.; Zhong, X. D.; Wang, X.; Yang, Y.; Wang, Z. L. Hybrid energy cell for simultaneously harvesting wind, solar, and chemical energies. *Nano Res.* **2014**, *7*, 1631–1639.

[12] Guo, H. Y.; Pu, X. J.; Chen, J.; Meng, Y.; Yeh, M. H.; Liu, G. L.; Tang, Q.; Chen, B. D.; Liu, D.; Qi, S. et al. A highly sensitive, self-powered triboelectric auditory sensor for social robotics and hearing aids. *Sci. Robot.* **2018**, *3*, eaat2516.

[13] Fu, X. P.; Bu, T. Z.; Li, C. L.; Liu, G. X.; Zhang, C. Overview of micro/nano-wind energy harvesters and sensors. *Nanoscale* **2020**, *12*, 23929–23944.
[14] Barrows, S. E.; Homer, J. S.; Orrell, A. C. Valuing wind as a distributed energy resource: A literature review. *Renew. Sust. Energy Rev.* **2021**, *152*, 111678.
[15] Hu, J.; Pu, X. J.; Yang, H. M.; Zeng, Q. X.; Tang, Q.; Zhang, D. Z.; Hu, C. G.; Xi, Y. A flutter-effect-based triboelectric nanogenerator for breeze energy collection from arbitrary directions and self-powered wind speed sensor. *Nano Res.* **2019**, *12*, 3018–3023.
[16] Ackermann, T.; Söder, L. Wind energy technology and current status: A review. *Renew. Sust. Energy Rev.* **2000**, *4*, 315–374.
[17] Wang, Z. L.; Jiang, T.; Xu, L. Toward the blue energy dream by triboelectric nanogenerator networks. *Nano Energy* **2017**, *39*, 9–23.
[18] Li, H. H.; Liang, C. J.; Ning, H.; Liu, J. Q.; Zheng, C. Y.; Li, J. Y.; Yao, H. L.; Peng, Y.; Wan, L. Y.; Liu, G. L. O-ring-modularized triboelectric nanogenerator for robust blue energy harvesting in all-sea areas. *Nano Energy* **2022**, *103*, 107812.
[19] Fan, F. R.; Tian, Z. Q.; Wang, Z. L. Flexible triboelectric generator. *Nano Energy* **2012**, *1*, 328–334.
[20] Liu, G. L.; Guo, H. Y.; Xu, S. X.; Hu, C. G.; Wang, Z. L. Oblate spheroidal triboelectric nanogenerator for all-weather blue energy harvesting. *Adv. Energy Mater.* **2019**, *9*, 1900801.
[21] Feng, J. R.; Zhou, H. L.; Cao, Z.; Zhang, E. Y.; Xu, S. X.; Li, W. T.; Yao, H. L.; Wan, L. Y.; Liu, G. L. 0.5 m triboelectric nanogenerator for efficient blue energy harvesting of all-sea areas. *Adv. Sci.* **2022**, *9*, 2204407.
[22] Yang, Y.; Zhu, G.; Zhang, H. L.; Chen, J.; Zhong, X. D.; Lin, Z. H.; Su, Y. J.; Bai, P.; Wen, X. N.; Wang, Z. L. Triboelectric nanogenerator for harvesting wind energy and as self-powered wind vector sensor system. *ACS Nano* **2013**, *7*, 9461–9468.
[23] Ren, Z. W.; Wang, Z. M.; Liu, Z. R.; Wang, L. F.; Guo, H. Y.; Li, L. L.; Li, S. T.; Chen, X. Y.; Tang, W.; Wang, Z. L. Energy harvesting from breeze wind (0.7–6 $m \cdot s^{-1}$) using ultra-stretchable triboelectric nanogenerator. *Adv. Energy Mater.* **2020**, *10*, 2001770.
[24] Zhao, Z. F.; Pu, X.; Du, C. H.; Li, L. X.; Jiang, C. Y.; Hu, W. G.; Wang, Z. L. Freestanding flag-type triboelectric nanogenerator for harvesting high-altitude wind energy from arbitrary directions. *ACS Nano* **2016**, *10*, 1780–1787.
[25] Chen, J.; Huang, Y.; Zhang, N. N.; Zou, H. Y.; Liu, R. Y.; Tao, C. Y.; Fan, X.; Wang, Z. L. Micro-cable structured textile for simultaneously harvesting solar and mechanical energy. *Nat. Energy* **2016**, *1*, 16138.
[26] Zhang, X. M.; Hu, J.; Yang, Q. X.; Yang, H. M.; Yang, H. K.; Li, Q. Y.; Li, X. C.; Hu, C. G.; Xi, Y.; Wang, Z. L. Harvesting multidirectional breeze energy and self-powered intelligent fire detection systems based on triboelectric nanogenerator and fluid-dynamic modeling. *Adv. Funct. Mater.* **2021**, *31*, 2106527.
[27] Xu, S. X.; Liu, G. L.; Wang, J. B.; Wen, H. G.; Cao, S.; Yao, H. L.; Wan, L. Y.; Wang, Z. L. Interaction between water wave and geometrical structures of floating triboelectric nanogenerators. *Adv. Energy Mater.* **2022**, *12*, 2103408.
[28] Wang, Y.; Yang, E.; Chen, T. Y.; Wang, J. Y.; Hu, Z. Y.; Mi, J. C.; Pan, X. X.; Xu, M. Y. A novel humidity resisting and wind direction adapting flag-type triboelectric nanogenerator for wind energy harvesting and speed sensing. *Nano Energy* **2020**, *78*, 105279.
[29] Wang, S. H.; Mu, X. J.; Yang, Y.; Sun, C. L.; Gu, A. Y.; Wang, Z. L. Flow-driven triboelectric generator for directly powering a wireless sensor node. *Adv. Mater.* **2015**, *27*, 240–248.
[30] Bae, J.; Lee, J.; Kim, S.; Ha, J.; Lee, B. S.; Park, Y.; Choong, C.; Kim, J. B.; Wang, Z. L.; Kim, H. Y. et al. Flutter-driven triboelectrification for harvesting wind energy. *Nat. Commun.* **2014**, *5*, 4929.
[31] Zou, H. X.; Zhao, L. C.; Wang, Q.; Gao, Q. H.; Yan, G.; Wei, K. X.; Zhang, W. M. A self-regulation strategy for triboelectric nanogenerator and self-powered wind-speed sensor. *Nano Energy* **2022**, *95*, 106990.
[32] Yong, S.; Wang, J. Y.; Yang, L. J.; Wang, H. Q.; Luo, H.; Liao, R. J.; Wang, Z. L. Auto-switching self-powered system for efficient broad-band wind energy harvesting based on dual-rotation shaft triboelectric nanogenerator. *Adv. Energy Mater.* **2021**, *11*, 2101194.
[33] Luo, Y. J.; Chen, P. F.; Cao, L. N. Y.; Xu, Z. J.; Wu, Y.; He, G. F.; Jiang, T.; Wang, Z. L. Durability improvement of breeze-driven triboelectric–electromagnetic hybrid nanogenerator by a travel-controlled approach. *Adv. Funct. Mater.* **2022**, *32*, 2205710.
[34] Zhao, K.; Sun, W. R.; Zhang, X. T.; Meng, J. K.; Zhong, M.; Qiang, L.; Liu, M. J.; Gu, B. N.; Chung, C. C.; Liu, M. C. et al. High-performance and long-cycle life of triboelectric nanogenerator using PVC/MoS_2 composite membranes for wind energy scavenging application. *Nano Energy* **2022**, *91*, 106649.
[35] Han, J. J.; Feng, Y. W.; Chen, P. F.; Liang, X.; Pang, H.; Jiang, T.; Wang, Z. L. Wind-driven soft-contact rotary triboelectric nanogenerator based on rabbit fur with high performance and durability for smart farming. *Adv. Funct. Mater.* **2022**, *32*, 2108580.
[36] Wang, J. Y.; Ding, W. B.; Pan, L.; Wu, C. S.; Yu, H.; Yang, L. J.; Liao, R. J.; Wang, Z. L. Self-powered wind sensor system for detecting wind speed and direction based on a triboelectric nanogenerator. *ACS Nano* **2018**, *12*, 3954–3963.
[37] Chen, J.; Guo, H. Y.; Hu, C. G.; Wang, Z. L. Robust triboelectric nanogenerator achieved by centrifugal force induced automatic working mode transition. *Adv. Energy Mater.* **2020**, *10*, 2000886.
[38] Li, S. M.; Wang, S. H.; Zi, Y. L.; Wen, Z.; Lin, L.; Zhang, G.; Wang, Z. L. Largely improving the robustness and lifetime of triboelectric nanogenerators through automatic transition between contact and noncontact working states. *ACS Nano* **2015**, *9*, 7479–7487.
[39] Long, L.; Liu, W. L.; Wang, Z.; He, W. C.; Li, G.; Tang, Q.; Guo, H. Y.; Pu, X. J.; Liu, Y. K.; Hu, C. G. High performance floating self-excited sliding triboelectric nanogenerator for micro mechanical energy harvesting. *Nat. Commun.* **2021**, *12*, 4689.
[40] Joselin Herbert, G. M.; Iniyan, S.; Sreevalsan, E.; Rajapandian, S. A review of wind energy technologies. *Renew. Sust. Energy Rev.* **2007**, *11*, 1117–1145.